The error propagation in the CBF and $CMRO_2$ values estimated in this study was based on the measured input functions obtained in the series of our PET study. The size of the error in these values might change, for example, if the $H_2^{15}O$ injection or $^{15}O_2$ inhalation period is changed. In particular, method (B) is highly dependent on the shape of the input function. Further studies are required to investigate how method (B) works when the shape of the input function is different from that of the input function we used here.

In the simulation, we used a 3 min time interval between the injections of the first and second tracers. This 3 min time interval was based on a previous simulation study (Iida *et al* 2002), which suggested that images of a quality equivalent to the 3SARG protocol could be obtained if the time interval was at least 3 min. Additionally, a 3 min scan duration for oxygen would provide reasonable image quality in CBF and $CMRO_2$ (Kudomi *et al* 2005).

In conclusion, this study demonstrates the feasibility of the separation of the dual tracer coexistent input function for rapid and simultaneous measurement of CBF and $CMRO_2$ using a single PET scan that accompanies the sequential administration of two tracers. The simulation studies showed that the present method for separation of the two components $H_2^{15}O$ and $^{15}O_2$ provides reasonable accuracy for the quantitative values of CBF, OEF and $CMRO_2$.

Acknowledgments

The authors gratefully acknowledge the staff of the Department of Nuclear Medicine, Hospital and the Department of Investigative Radiology, Research Institute, National Cardiovascular Center. The present work was supported by the Program for Promotion of Fundamental Studies in Health Science of the Organization for Pharmaceuticals and Medical Devices Agency of Japan (PMDA), by Nakatani Electronic Measuring Technology Association of Japan, and by the Program for Promotion of Fundamental Studies in Health Science of the Organization for Pharmaceutical Safety and Research (of Japan).

References

Correia J A, Alpert N M, Buxton R B and Ackerman R H 1985 Analysis of some errors in the measurement of oxygen extraction and oxygen consumption by the equilibrium inhalation method *J. Cereb. Blood Flow Metab.* **5** 591–9

Eriksson L, Holte S, Bohm C, Kesselberg M and Hovander B 1988 Automated blood sampling system for positron emission tomography *IEEE Trans. Nucl. Sci.* **35** 703–7

Eriksson L and Kanno I 1991 Blood sampling devices and measurements *Med. Prog. Technol.* **17** 249–57

Frackowiak R S, Jones T, Lenzi G L and Heather J D 1980a Regional cerebral oxygen utilization and blood flow in normal man using oxygen-15 and positron emission tomography *Acta Neurol. Scand.* **62** 336–44

Frackowiak R S, Lenzi G L, Jones T and Heather J D 1980b Quantitative measurement of regional cerebral blood flow and oxygen metabolism in man using 15O and positron emission tomography: theory, procedure, and normal values *J. Comput. Assist. Tomogr.* **4** 727–36

Fujita H, Kuwabara H, Reutens D C and Gjedde A 1999 Oxygen consumption of cerebral cortex fails to increase during continued vibrotactile stimulation *J. Cereb. Blood Flow Metab.* **19** 266–71

Hatazawa J *et al* 1995 Regional cerebral blood flow, blood volume, oxygen extraction fraction, and oxygen utilization rate in normal volunteers measured by the autoradiographic technique and the single breath inhalation method *Ann. Nucl. Med.* **9** 15–21

Hattori N, Bergsneider M, Wu H M, Glenn T C, Vespa P M, Hovda D A, Phelps M E and Huang S C 2004 Accuracy of a method using short inhalation of 15O–O2 for measuring cerebral oxygen extraction fraction with PET in healthy humans *J. Nucl. Med.* **45** 765–70

Hayashi T, Watabe H, Kudomi N, Kim K M, Enmi J, Hayashida K and Iida H 2003 A theoretical model of oxygen delivery and metabolism for physiologic interpretation of quantitative cerebral blood flow and metabolic rate of oxygen *J. Cereb. Blood Flow Metab.* **23** 1314–23

Herscovitch P, Markham J and Raichle M E 1983 Brain blood flow measured with intravenous $H_2^{15}O$: I. Theory and error analysis *J. Nucl. Med.* **24** 782–9

Ho D and Feng D 1999 Rapid algorithms for the construction of cerebral blood flow and oxygen utilization images with oxygen-15 and dynamic positron emission tomography *Comput. Methods Prog. Biomed.* **58** 99–117

Holden J E, Eriksson L, Roland P E, Stone-Elander S, Widen L and Kesselberg M 1988 Direct comparison of single-scan autoradiographic with multiple-scan least-squares fitting approaches to PET $CMRO_2$ estimation *J. Cereb. Blood Flow Metab.* **8** 671–80

Huang S C, Feng D G and Phelps M E 1986 Model dependency and estimation reliability in measurement of cerebral oxygen utilization rate with oxygen-15 and dynamic positron emission tomography *J. Cereb. Blood Flow Metab.* **6** 105–19

Iida H, Higano S, Tomura N, Shishido F, Kanno I, Miura S, Murakami M, Takahashi K, Sasaki H and Uemura K 1988 Evaluation of regional differences of tracer appearance time in cerebral tissues using [^{15}O] water and dynamic positron emission tomography *J. Cereb. Blood Flow Metab.* **8** 285–8

Iida H, Jones T and Miura S 1993 Modeling approach to eliminate the need to separate arterial plasma in oxygen-15 inhalation positron emission tomography *J. Nucl. Med.* **34** 1333–40

Iida H, Kanno I, Miura S, Murakami M, Takahashi K and Uemura K 1986 Error analysis of a quantitative cerebral blood flow measurement using H2(15)O autoradiography and positron emission tomography, with respect to the dispersion of the input function *J. Cereb. Blood Flow Metab.* **6** 536–45

Iida H, Miyake Y, Hayashi T, Kudomi N, Ogawa M, Teramoto N, Kim K M, Oka H and Hayashida K 2002 A new strategy for rapid clinical imaging of $rCMRO_2$, rCBF and rOEF using PET *J. Nucl. Med.* **43** 62P

Iida H *et al* 2000 Quantitation of regional cerebral blood flow corrected for partial volume effect using O-15 water and PET: I. Theory, error analysis, and stereologic comparison *J. Cereb. Blood Flow Metab.* **20** 1237–51

Kanno I *et al* 1987 A system for cerebral blood flow measurement using an $H_2^{15}O$ autoradiographic method and positron emission tomography *J. Cereb. Blood Flow Metab.* **7** 143–53

Kudomi N Choi C, Watabe H, Kim K M, Shidahara M, Ogawa M, Teramoto N, Sakamoto E and Iida H 2003 Development of a GSO detector assembly for a continuous blood sampling system *IEEE Trans. Nucl. Sci.* **50** 70–3

Kudomi N, Hayashi T, Teramoto N, Watabe H, Kawachi N, Ohta Y, Kim K M and Iida H 2005 Rapid quantitative measurement of $CMRO_2$ and CBF by dual administration of ^{15}O-labelled oxygen and water during a single PET scan-a validation study and error analysis in anesthetized monkeys *J. Cereb. Blood Flow Metab.* **25** 1209–24

Lammertsma A A, Cunningham V J, Deiber M P, Heather J D, Bloomfield P M, Nutt J, Frackowiak R S and Jones T 1990 Combination of dynamic and integral methods for generating reproducible functional CBF images *J. Cereb. Blood Flow Metab.* **10** 675–86

Lammertsma A A, Heather J D, Jones T, Frackowiak R S and Lenzi G L 1982 A statistical study of the steady state technique for measuring regional cerebral blood flow and oxygen utilisation using 15O *J. Comput. Assist. Tomogr.* **6** 566–73

Lammertsma A A and Jones T 1983 Correction for the presence of intravascular oxygen-15 in the steady-state technique for measuring regional oxygen extraction ratio in the brain: 1. Description of the method *J. Cereb. Blood Flow Metab.* **3** 416–24

Meyer E, Tyler J L, Thompson C J, Redies C, Diksic M and Hakim A M 1987 Estimation of cerebral oxygen utilization rate by single-bolus $^{15}O_2$ inhalation and dynamic positron emission tomography *J. Cereb. Blood Flow Metab.* **7** 403–14

Mintun M A, Raichle M E, Martin W R and Herscovitch P 1984 Brain oxygen utilization measured with O-15 radiotracers and positron emission tomography *J. Nucl. Med.* **25** 177–87

Mintun M A, Vlassenko A G, Shulman G L and Snyder A Z 2002 Time-related increase of oxygen utilization in continuously activated human visual cortex *Neuroimage* **16** 531–7

Ohta S, Meyer E, Thompson C J and Gjedde A 1992 Oxygen consumption of the living human brain measured after a single inhalation of positron emitting oxygen *J. Cereb. Blood Flow Metab.* **12** 175–92

Okazawa H, Yamauchi H, Sugimoto K, Takahashi M, Toyoda H, Kishibe Y and Shio H 2001a Quantitative comparison of the bolus and steady-state methods for measurement of cerebral perfusion and oxygen metabolism: positron emission tomography study using 15O-gas and water *J. Cereb. Blood Flow Metab.* **21** 793–803

Okazawa H, Yamauchi H, Sugimoto K, Toyoda H, Kishibe Y and Takahashi M 2001b Effects of acetazolamide on cerebral blood flow, blood volume, and oxygen metabolism: a positron emission tomography study with healthy volunteers *J. Cereb. Blood Flow Metab.* **21** 1472–9

Raichle M E, Martin W R, Herscovitch P, Mintun M A and Markham J 1983 Brain blood flow measured with intravenous $H_2^{15}O$: II. Implementation and validation *J. Nucl. Med.* **24** 790–8

Sadato N, Yonekura Y, Senda M, Iwasaki Y, Matoba N, Tamaki N, Sasayama S, Magata Y and Konishi J 1993 PET and the autoradiographic method with continuous inhalation of oxygen-15-gas: theoretical analysis and comparison with conventional steady-state methods *J. Nucl. Med.* **34** 1672–80

Shidahara M *et al* 2002 Evaluation of a commercial PET tomograph-based system for the quantitative assessment of rCBF, rOEF and rCMRO$_2$ by using sequential administration of ^{15}O-labelled compounds *Ann. Nucl. Med.* **16** 317–27

Subramanyam R, Alpert N M, Hoop B Jr, Brownell G L and Taveras J M 1978 A model for regional cerebral oxygen distribution during continuous inhalation of $^{15}O_2$, C^{15}O, and C$^{15}15O_2$ *J. Nucl. Med.* **19** 48–53

Vafaee M S and Gjedde A 2000 Model of blood-brain transfer of oxygen explains nonlinear flow-metabolism coupling during stimulation of visual cortex *J. Cereb. Blood Flow Metab.* **20** 747–54

Votaw J R and Shulman S D 1998 Performance evaluation of the Pico-count flow-through detector for use in cerebral blood flow PET studies *J. Nucl. Med.* **39** 509–15

Original article

Nuclear Medicine Communications

Body-contour versus circular orbit acquisition in cardiac SPECT: Assessment of defect detectability with channelized Hotelling observer

Antti Sohlberg[a], Hiroshi Watabe[a], Miho Shidahara[b] and Hidehiro Iida[a]

Background **The resolution of a gamma camera is depth-dependent and worsens with increasing distance to the camera resulting in a loss of fine details in SPECT images. A common approach to reduce the effects of this resolution loss is to utilize body-contour acquisition orbits. Even though body-contour orbits can improve resolution of reconstructed images their effect on lesion detection is not well known.**

Objective **To investigate whether body-contour orbits offer better defect detection performance than circular orbits in cardiac SPECT.**

Methods **The mathematical cardiac torso (MCAT) phantom was used to model ^{99m}Tc-sestamibi uptake. A total of four phantoms (two male and two female) with eight defects (four locations and two sizes) were generated and projection data were simulated using an analytical projector with attenuation, scatter, collimator response and acquisition orbit modelling. The circular and body-contour projections were reconstructed using the OSEM algorithm with/without collimator response compensation. Defect detection performance was assessed by calculating area under the receiver operating characteristic (ROC) curve for channelized Hotelling observer.**

Results **The defect detection performance of circular and body-contour acquisition was very similar and the difference in the area under the ROC curve between the orbits was not statistically significant with or without collimator response compensation. The collimator response compensation, on the other hand, was noticed to be valuable and it provided significantly better defect detection performance than reconstruction without it regardless of the acquisition orbit type.**

Conclusions **We conclude that by replacing circular orbit with more complex body-contour orbit will not lead to statistically significant increase in defect detection performance in cardiac SPECT. *Nucl Med Commun* 28:937–942 © 2007 Wolters Kluwer Health | Lippincott Williams & Wilkins.**

Nuclear Medicine Communications 2007, 28:937–942

Keywords: body-contour orbit, cardiac SPECT, circular orbit

[a]National Cardiovascular Center Research Institute, Osaka, Japan and [b]Molecular Imaging Center, National Institute of Radiological Sciences, Chiba, Japan

Correspondence to Dr Antti Sohlberg, National Cardiovascular Center Research Institute, 5-7-1, Fujishiro-dai, Suita City, Osaka 565-8565, Japan
Tel: +81 6833 5012 (ext. 2559); fax: +81 6 6835 5429;
e-mail: antti@ri.ncvc.go.jp

Received 28 May 2007 Revised 31 July 2007
Accepted 31 August 2007

Introduction

The resolution of a gamma camera is depth dependent, which results in a loss of fine details in SPECT images. In order to reduce the effects of this depth dependency, body-contour acquisition orbits are often applied. Body-contour orbits improve the resolution by minimizing the object-to-detector distance and can provide approximately 1–2 mm improvement in resolution without any loss in sensitivity, when projection data is acquired with parallel hole collimators. Utilization of body-contour orbits is, however, complicated by the more complex acquisition process, especially if automatic contour tracking is used, and by the fact that body-contour orbits might be more prone to image artefacts than circular orbits [1,2]. These artefacts are generated due to resolution non-uniformity among different projections and their severity depends on the geometry of the orbit and also on orientation of the target in the field of view [3,4].

Another approach to reduce the depth-dependent blurring is to apply collimator response compensation in reconstruction. Several investigators have indicated that significant improvements in image quality can be achieved when collimator response compensation is applied during reconstruction [5–8]. Collimator response modelling might also be beneficial when combined with body-contour orbits, because in addition to its resolution enhancement capabilities collimator response correction increases uniformity of resolution and could therefore reduce the artefacts, which have been reported to reduce the quality of body-contour studies.

Image quality obtained with different acquisition and reconstruction configurations is usually assessed with traditional metrics such as resolution and contrast. Even though these metrics are easy to apply and understand they are not necessarily good predictors of defect detection performance, which is the primary concern in cardiac SPECT. In this study the channelized Hotelling observer (CHO), which has shown to correlate well with human observer performance [9], was used to compare body-contour and circular orbits with and without collimator response compensation. The goal was to determine whether body-contour orbits could offer better defect detection performance in cardiac SPECT studies than circular orbits and to find the optimal acquisition–reconstruction method combination.

Materials and methods

Phantoms

The mathematical cardiac torso (MCAT) phantom [10,11] was used to simulate ^{99m}Tc-sestamibi distribution and non-uniform attenuation in the chest region. Four different phantoms, large female/male and small female/male, were generated each with eight different defects (Fig. 1). The lateral and antero-posterior sizes were 38 cm and 26 cm for the large phantoms and 32 cm and 24 cm for the small phantoms. The relative activities per voxel assigned to myocardium, liver, kidney, spleen, lung and rest of the body were 100, 50, 100, 80, 5 and 2.5. The defects had 90° or 120° angular extent, approximately 2.5 cm length and they were simulated with 20% contrast with respect to healthy myocardium.

Projection data simulation

Noise-free projection data was simulated using an analytical projector. Attenuation was simulated with the MCAT attenuation maps and collimator response was modelled according to the method by Metz [12]. A high-resolution low-energy parallel hole collimator with 4.0 cm hole length and 0.18 cm hole radius was used in the simulations. Circular hole shape was assumed which allowed the collimator point-spread function to be calculated analytically according to:

$$g(r,D) = 2\cos^{-1}\left(\frac{|r_T|}{2R}\right) - \frac{|r_T|}{R}\sqrt{1-\frac{|r_T|^2}{4R^2}}, \quad (1)$$

where r is the distance in the detection plane from the intersection of the line perpendicular to the detection plane containing the source, D perpendicular distance from collimator to the source, R the radius of collimator hole and r_T the displacement of the centres of the projected aperture functions from the front face and back face of the collimator [13]. r_T is given by

$$r_T = r\frac{L}{D+L+C}, \quad (2)$$

where L is the collimator hole length and C the distance from back of the collimator to the detector crystal. Scatter was included using the method by Hutton [14,15]. Hutton's method consists of three steps. In the

Fig. 1

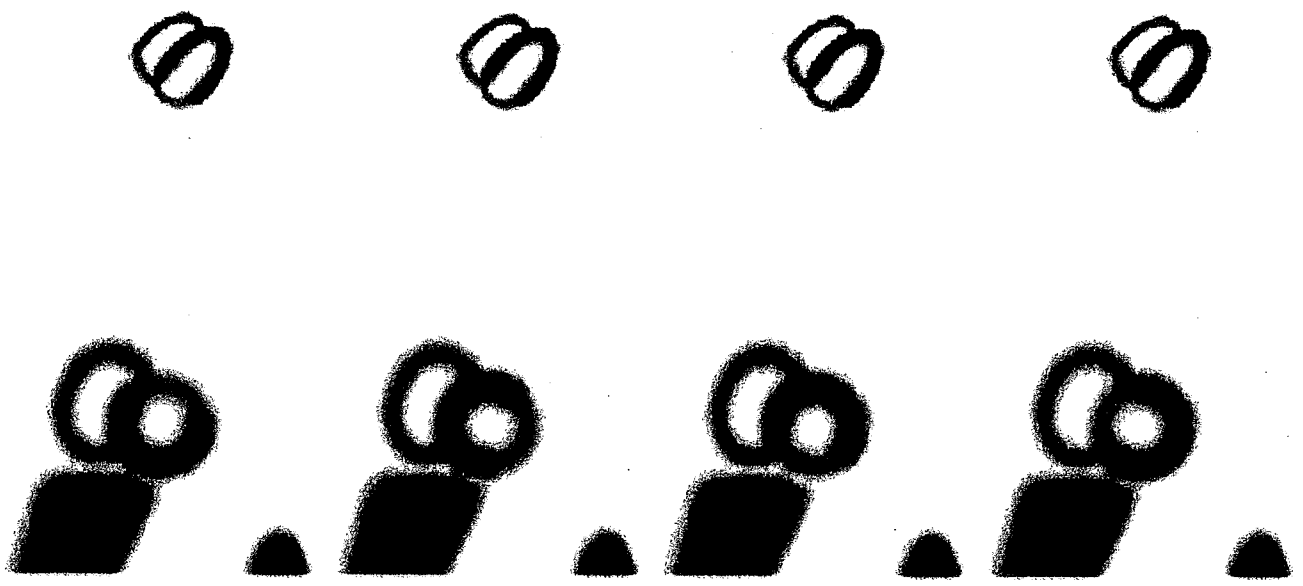

Top row: Example transverse slices of the MCAT phantoms used in the simulations. Bottom row: Example short-axis slices illustrating defect locations (defect contrast was enhanced for displaying purposes).

first step the activity distribution is convolved with monoexponential scatter kernels (exp $\alpha(d_s)r_s$), whose slopes $\alpha(d_s)$ depend on the depth in tissue (d_s). In the second step the convolved emission distribution is scaled using transmission-dependent scatter-to-true scatter fraction SF:

$$\mathrm{SF} = A - B\left(e^{-\sum_{k=j}^{skin}\mu_k\Delta}\right)^{\gamma} - 1, \qquad (3)$$

where μ_k is the linear attenuation coefficient for voxel k, Δ the voxel size and parameters A, B and γ are fitting parameters obtained from experiment [14]. Scatter projections are finally obtained in the third step by forward projecting the convolved and scaled activity distribution at each projection angle.

Projection data was generated for 128 angles over 360° arc using 256 × 256 projection matrix and 0.156 cm pixel size. The radius of rotation for the body-contour orbits, at each projection angle, was determined by tracking the distance from the centre of rotation to the surface of the attenuation map of each four phantoms and circular orbit's radius of rotation was set to the maximum radius found in the corresponding body-contour orbit study. After simulation the projections were collapsed into 64 × 64 matrix size and Poisson noise was added. Projections were scaled so that the number of total counts was approximately 3.0 MCts. A total of 480 noisy projection data sets (four phantoms × eight defects × 15 noise realizations) with defect and 480 projection data sets (four phantoms × 120 noise realizations) without defect were generated for both orbits.

Reconstruction and post-processing

Reconstructions were performed using OSEM algorithm [16]. The projectors in our OSEM implementation were rotation based [17] and the rotation was performed using bilinear interpolation. Attenuation correction was included into the algorithm by rotating the attenuation map with the reconstruction volume during the reconstruction and applying each voxel the appropriate attenuation factor, which was calculated by summing the attenuation map along perpendicular lines from the volume elements to the detector. Original attenuation maps were blurred using a three-dimensional (3-D) Gaussian kernel with 1.0 cm full width at half maximum (FWHM) before they were applied in reconstruction in order to make attenuation compensation more realistic. Collimator response compensation was implemented by blurring each image plane at a different distance from the detector with a separable two-dimensional Gaussian kernel, whose FWHM was calculated assuming a linear model

$$\mathrm{FWHM}(D) = \alpha + \beta D, \qquad (4)$$

for the decrease of resolution as a function of distance (D) from the detector. The α and β parameters were obtained by simulating point sources at different distance from the collimator using the analytic projector described in previous section. FWHMs of these measurements were calculated and the linear model in Equation 4 was fitted to the measurements. It is worthwhile to note that collimator response compensation was performed using a different method that was used to simulate the projection data. This approach should provide more realistic results with collimator correction, which are not 'too good' due to the complete match of the projectors used in generation of the projection data and reconstruction. Correction for scatter was not performed.

Every noisy circular and body-contour projection data set was reconstructed with/without collimator response compensation using 32 subsets and two iterations. Reconstructed images were post-filtered with 3-D Gaussian filter with 1.25 cm FWHM. These reconstruction/post-filtering parameters have shown to provide near optimal defect detection performance in previous studies [18,19]. After filtering, images were realigned into short-axis slices and a single slice through the centre of the defect (for defect absent images the corresponding slice) was extracted for further analysis.

Channelized Hotelling observer and receiver operating characteristic analysis

Defect detection performance is most often measured using human observers. In these studies observers are shown a large number of images with and without defects acquired/reconstructed using the methods, which are to be compared against each other. The observers rate the existence of a defect, e.g., with a continuous scale from 0 (defect definitely absent) to 100 (defect definitely present). These ratings are then used to generate a receiver operating characteristic (ROC) curves, which plot the true positive fraction (fraction of images correctly classified as defect present) of the ratings against the false positive fraction (fraction of images falsely classified as defect present). The area under the ROC curve can be used as a measure of defect detection performance. The human observer studies are, however, often too time-consuming and expensive to perform and therefore computer observers such as the channelized Hotelling observer have been developed.

The CHO comes from signal-detection theory and its derivation is beyond the scope of this paper, but can be found elsewhere [20]. The following explains how CHO was applied in this work. The test statistic (λ), which is analogous to the rating obtained in a human observer study, was calculated for the CHO as

$$\lambda = h^{\mathrm{T}} \bullet g, \qquad (5)$$

where h^{T} is the CHO, g is the feature vector and superscript T denotes transpose operation. The feature vector was obtained by processing the short-axis slice under testing by frequency selective channels, which

have been added to computer observers to mimic human visual processing of images [18]. In this study four rotationally symmetric channels with 1/64–2/64, 2/64–4/64, 4/64–8/64 and 8/64–16/64 cycles/pixel passbands were used. The frequency channels were shifted to each defect centre (shift was performed also for defect absent images) with a phase shift and the channels were converted into spatial domain with inverse Fourier transform. The CHO was calculated as

$$h^{\mathrm{T}} = (\langle g_1 \rangle - \langle g_2 \rangle)^{\mathrm{T}} S_{II}^{-1}, \qquad (6)$$

where $\langle g_1 \rangle$ is the mean feature vector for defect present images, $\langle g_2 \rangle$, mean feature vector for defect absent images and S_{II} the intraclass scatter matrix [18,21]. First half of the short axis slices for each orbit/reconstruction method combination were used to calculate the CHO and the remaining half of the images were used to obtain the actual test statistics. Each receiver operating characteristic (ROC) curve was therefore estimated from the rating data of 240 defects present (four phantoms × eight defects × 15 noise realizations ÷ 2) and 240 defect absent (four phantoms × 120 noise realizations ÷ 2) images. The ROC curves and areas under the curves (AUC) were obtained using the ROCKIT software (http://www-radiology.uchicago.edu/krl).

Results

The results of the acquisition orbit comparison are presented in Table 1 and Fig. 2. As can be seen body-contour orbit offers slightly better defect detection performance than circular orbit when collimator response compensation is not applied, but the difference in the AUC values between the two orbits is not statistically significant at $P = 0.05$ level. Interestingly circular orbit performs better with collimator response correction than body-contour acquisition. This is probably due to the fact that the reconstruction voxel size is quite large compared to the FWHM of the Gaussian that is used to model the collimator response, which might lead to relatively crude presentation of the blurring kernels. With body-contour orbits this phenomenon has even bigger effect, because the imaging distance is shorter and thus the Gaussian kernels are narrower. It is, however, important to note that the difference in AUCs between circular and body-contour orbits when collimator response compensation is applied is not statistically significant.

Table 1 Comparison between circular/body-contour acquisition and reconstruction with/without collimator response compensation (coll)

Method 1	Method 2	AUC 1	AUC 2	*P*
Circular w/o coll	Contour w/o coll	0.856	0.862	0.358
Circular w coll	Contour w coll	0.901	0.894	0.325
Circular w/o coll	Circular w coll	0.856	0.901	<0.001
Contour w/o coll	Contour w coll	0.862	0.894	<0.001

Fig. 2

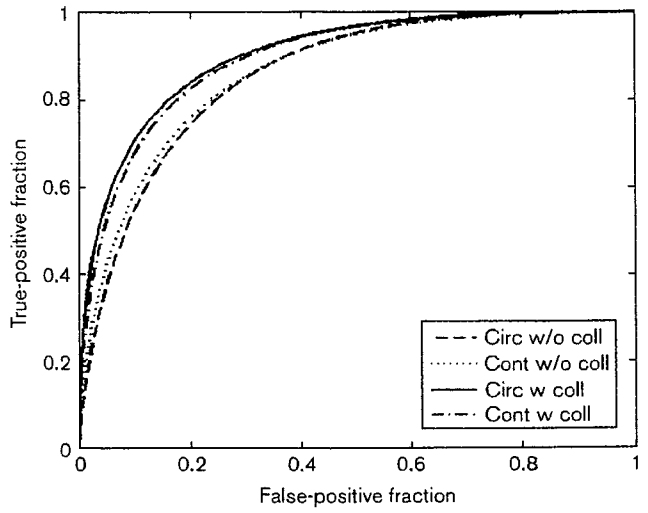

ROC curves for circular and body-contour orbit studies reconstructed with/without collimator response compensation (coll).

Figure 3 shows representative images from circular and body-contour orbit studies. When comparing individual images it is worthwhile keeping in mind that circular and body-contour images correspond to different projection data noise realizations and thus some of the differences seen in images might be due to noise and not different acquisition orbits. Overall there are no large differences among the images. Reconstructions with collimator response compensation provide smoother and thus perhaps more visually pleasing image quality than reconstruction without correction.

Discussion

Body-contour acquisition orbits have the ability to increase resolution and contrast, but their effect on defect detection performance in cardiac SPECT is not well known. This study compared circular and body-contour orbits using CHO and ROC analysis. The defect detectability with the two orbits was noticed to be quite similar. The difference in areas under the ROC curve was 0.006 for reconstruction without collimator modelling and 0.007 with collimator modelling. Even though the body-contour orbit increased the area under curve, when collimator response correction was not applied, it could not provide statistically significant improvement in defect detection performance. Similar findings were made by White *et al.* [22], who reported that circular and body-contour orbits do not differ significantly in terms of defect extent, reversibility or size assessment.

Body-contouring adds extra complexity to acquisition procedure and may generate additional artefacts as

Fig. 3

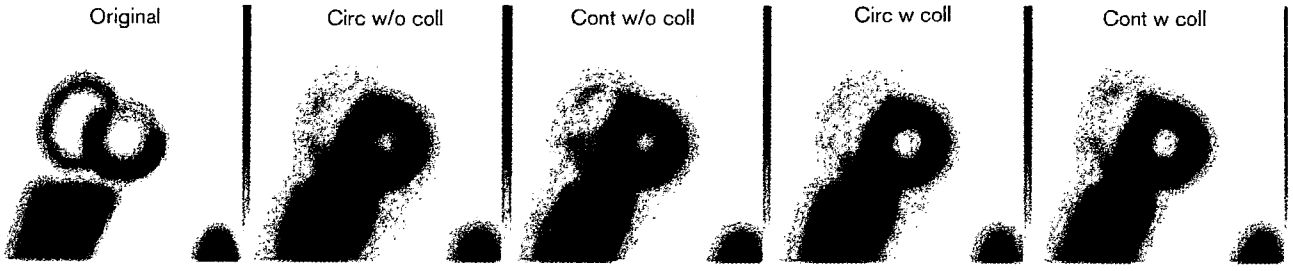

Example reconstructed short-axis slices obtained with circular and body-contour orbit with/without collimator response compensation (coll). Original image has enhanced defect contrast.

explained in Introduction. We proposed that collimator response modelling might reduce these artefacts and could therefore offer better image quality. No significant acquisition orbit related artefacts were, however, noticed in this study. The absence of artefacts might be partly related to the utilization of 360° acquisitions orbits, which have shown to be less prone to errors than 180° orbits [1]. Moreover, many of the studies that have reported artefacts with body-contour orbits have used filtered back-projection (FBP) as reconstruction method, whereas we used OSEM, which is known to provide images with higher quality than FBP. Even though the body-contour orbit and collimator response compensation combination did not outperform circular orbit with collimator response correction, the collimator response compensation itself was noticed to be very valuable. Collimator response correction increased AUC by 0.045 for circular and by 0.032 for body-contour orbit. Both improvements were statistically significant. Similar findings have been presented before [23,24].

This study has three primary limitations, which are discussed next. First the acquisition orbit comparison was performed using simulated rather than real patient data and thus might not provide the level of realism of a clinical study. On the other hand the complete lack of patient motion and other such factors that deteriorate the quality of clinical SPECT studies allowed us to concentrate only to differences due to acquisition orbits. Moreover, the exact knowledge of the size, shape and location of the defects made the detection performance measurements reliable. This investigation would have been quite difficult to perform as a clinical study: In order to obtain statistically reliable results a large patient population with, for example, angiography information would have been needed. Each patient participating in the study would have also needed two sequential SPECT scans, which would have increased patient discomfort and risk for motion artefacts, in addition to halving the throughput of our scanner.

Second, the simulations in this study were performed using an analytical projection code instead of a Monte Carlo simulator. An analytical simulator was chosen because many of the Monte Carlo packages available do not directly support acquisitions with non-symmetrical body-contour orbits. Our analytical simulator, on the other hand, allows easy modelling of the acquisition orbit. The collimator response modelling in our simulator is performed using similar method as with the popular SIMIND [25] and SIMSET [26] Monte Carlo packages. Thus the only larger difference between our analytical and Monte Carlo simulators is the incorporation of scatter. Scatter modelling in our simulator was implemented using Hutton's method and although this method produces relatively crude scatter approximation it still increases the realism of the projection data. We also believe that accurate scatter modelling is not so important in this study, because we are studying resolution effects.

Third, the image quality was assessed using computer observer instead of human observers. We chose computer observers, because human observer studies are time-consuming and expensive to perform. The CHO used in this work has, however, shown to correlate well with human observers [9,27]. CHOs can also provide much better prediction of human performance than metrics like resolution, contrast and noise level, which are often used to compare acquisition and reconstruction methods.

In conclusion, circular and body-contour orbits offer quite similar defect detection performance and thus the selection of acquisition orbit is of not vital importance in cardiac SPECT. Collimator response compensation, on the other hand, significantly increases defect detectability regardless of acquisition type and should therefore be applied in reconstruction whenever available.

Acknowledgement

This work was supported by grants from Japan Society for the Promotion of Science.

References

1 Eisner RL, Nowak DJ, Pettigrew R, Fajman W. Fundamentals of 180° acquisition and reconstruction in SPECT imaging. *J Nucl Med* 1986; **27**:1717–1728.

2 O'Connor MK, Hruska CB. Effect of tomographic orbit and type of rotation on apparent myocardial activity. *Nucl Med Commun* 2005; **26**:25–30.

3 Maniawski PJ, Morgan HT, Wackers FJT. Orbit-related variation in spatial resolution as a source of artifactual defects in thallium-201 SPECT. *J Nucl Med* 1991; **32**:871–875.

4 Abufadel A, Eisner RL, Schafer RW. Differences due to collimator blurring in cardiac images with use of circular and elliptic camera orbits. *J Nucl Cardiol* 2001; **8**:458–465.

5 Hutton BF, Lau YH. Application of distance-dependent resolution compensation and post-reconstruction filtering for myocardial SPECT. *Phys Med Biol* 1998; **43**:1679–1693.

6 Lau YH, Hutton BF, Beekman FJ. Choice of collimator for cardiac SPET when resolution compensation is included in iterative reconstruction. *Eur J Nucl Med* 2001; **28**:39–47.

7 Zeng GL, Gullberg GT. Frequency domain implementation of the three-dimensional geometric point response correction in SPECT imaging. *IEEE Trans Nucl Sci* 1992; **39**:1444–1453.

8 Zeng GL, Gullberg GT, Bai C, Christian PE, Trisjono F, Di Bella EVR, *et al.* Iterative reconstruction of fluorine-18 SPECT using geometric point response correction. *J Nucl Med* 1998; **39**:124–130.

9 Wollenweber SD, Tsui BMW, Lalush DS, Frey EC, LaCroix KJ, Gullberg GT. Comparison of Hotelling observer models and human observers in defect detection from myocardial SPECT imaging. *IEEE Trans Nucl Sci* 1999; **46**:2098–2103.

10 Tsui BMW, Zhao XD, Gregoriou GK, Lalush DS, Frey EC, Johnston RE, *et al.* Quantitative cardiac SPECT reconstruction with reduced image degradation due to patient anatomy. *IEEE Trans Nucl Med* 1994; **41**:2838–2844.

11 Pretorius PH, King MA, Tsui BMW, LaCroix KJ, Xia W. A mathematical model of motion of the heart for use in generating source and attenuation maps for simulating emission imaging. *Med Phys* 1999; **26**:2323–2332.

12 Metz CE, Atkins FB, Beck RN. The geometric transfer function component for scintillation camera collimators with straight parallel holes. *Phys Med Biol* 1980; **25**:1059–1070.

13 Frey EC, Tsui BMW, Gullberg GT. Improved estimation of the detector response function for converging beam collimators. *Phys Med Biol* 1998; **43**:941–950.

14 Hutton BF, Osiecki A, Meikle SR. Transmission-based scatter correction of 180° myocardial single-photon emission tomographic studies. *Eur J Nucl Med* 1996; **23**:1300–1308.

15 Hutton BF, Baccarne V. Efficient scatter modelling for incorporation in maximum likelihood reconstruction. *Eur J Nucl Med* 1998; **25**:1658–1665.

16 Hudson HM, Larkin RS. Accelerated image reconstruction using ordered subsets of projection data. *IEEE Trans Med Imag* 1994; **13**:601–609.

17 Di Bella EVR, Barclay AB, Eisner RL, Schafer RW. A comparison of rotation-based methods for iterative reconstruction algorithms. *IEEE Trans Nucl Sci* 1996; **43**:3370–3376.

18 Frey EC, Gilland KL, Tsui BMW. Application of task-based measures of image quality to optimization and evaluation of three-dimensional reconstruction-based compensation methods in myocardial perfusion SPECT. *IEEE Trans Med Imag* 2002; **21**:1040–1050.

19 Narayanan MV, Gifford HC, King MA, Pretorius PH, Farncombe TH, Bruyant P, *et al.* Optimization of iterative reconstructions of ^{99m}Tc cardiac SPECT studies using numerical observers. *IEEE Trans Nucl Sci* 2002; **5**:2355–2360.

20 Myers KJ, Barrett HH. Addition of a channel mechanism to the ideal-observer model. *J Opt Soc Am A* 1987; **4**:2447–2457.

21 Shidahara M, Inoue K, Maruyama M, Watabe H, Taki Y, Goto R, *et al.* Predicting human performance by channelized Hotelling observer in discriminating between Alzheimer's dementia and controls using statistically processed brain perfusion SPECT. *Ann Nucl Med* 2006; **20**:605–613.

22 White MP, Russell A, Mascitelli VA, Morris RS, Shehata AR, Heller GV. Clinical comparison of circular versus noncircular acquisition using technetium-99m myocardial perfusion SPECT imaging. *J Nucl Med Technol* 1997; **25**:37–40.

23 He X, Links JM, Gilland GL, Tsui BMW, Frey EC. Comparison of 180° and 360° acquisition for myocardial perfusion SPECT with compensation for attenuation, detector response, and scatter: Monte Carlo and mathematical observer results. *J Nucl Cardiol* 2006; **13**:345–353.

24 Narayanan MV, King MA, Pretorius PH, Dahlberg ST, Spencer F, Simon E, *et al.* Human-observer receiver-operating-characteristic evaluation of attenuation, scatter, and resolution compensation strategies for ^{99m}Tc myocardial perfusion imaging. *J Nucl Med* 2003; **44**:1725–1734.

25 Ljungberg M, Strand S-E. A Monte Carlo program for the simulation of scintillation camera characteristics. *Comput Methods Programs Biomed* 1989; **29**:257–272.

26 Harrison RL, Vannoy SD, Haynor DR, Gillispie SB, Kaplan MS, Lewellen TK. Preliminary experience with the photon history generator module of a public-domain simulation system for emission tomography. *Conf Rec IEEE Nucl Sci Symp* 1993; 1154–1158.

27 Sankaran S, Frey EC, Gilland KL, Tsui BMW. Optimum compensation method and filter cutoff frequency in myocardial SPECT: a human observer study. *J Nucl Med* 2002; **43**:432–438.

Ann Nucl Med (2007) 21:537–543
DOI 10.1007/s12149-007-0057-4

TECHNICAL NOTE

Accelerated 3D-OSEM image reconstruction using a Beowulf PC cluster for pinhole SPECT

Tsutomu Zeniya · Hiroshi Watabe · Antti Sohlberg
Hidehiro Iida

Received: 18 May 2007 / Accepted: 6 August 2007

Abstract
Objective A conventional pinhole single-photon emission computed tomography (SPECT) with a single circular orbit has limitations associated with non-uniform spatial resolution or axial blurring. Recently, we demonstrated that three-dimensional (3D) images with uniform spatial resolution and no blurring can be obtained by complete data acquired using two-circular orbit, combined with the 3D ordered subsets expectation maximization (OSEM) reconstruction method. However, a long computation time is required to obtain the reconstruction image, because of the fact that 3D-OSEM is an iterative method and two-orbit acquisition doubles the size of the projection data. To reduce the long reconstruction time, we parallelized the two-orbit pinhole 3D-OSEM reconstruction process by using a Beowulf personal computer (PC) cluster.
Methods The Beowulf PC cluster consists of seven PCs connected to Gbit Ethernet switches. Message passing interface protocol was utilized for parallelizing the reconstruction process. The projection data in a subset are distributed to each PC. The partial image forward- and back-projected in each PC is transferred to all PCs. The current image estimate on each PC is updated after summing the partial images. The performance of parallelization on the PC cluster was evaluated using two independent projection data sets acquired by a pinhole SPECT system with two different circular orbits.
Results Parallelization using the PC cluster improved the reconstruction time with increasing number of PCs. The reconstruction time of 54 min by the single PC was decreased to 10 min when six or seven PCs were used. The speed-up factor was 5.4. The reconstruction image by the PC cluster was virtually identical with that by the single PC.
Conclusions Parallelization of 3D-OSEM reconstruction for pinhole SPECT using the PC cluster can significantly reduce the computation time, whereas its implementation is simple and inexpensive.

Keywords Pinhole SPECT · Image reconstruction · 3D-OSEM · PC cluster · Parallel computing

T. Zeniya (✉) · H. Watabe · A. Sohlberg · H. Iida
Department of Investigative Radiology, Advanced Medical Engineering Center, National Cardiovascular Center Research Institute, 5-7-1 Fujishiro-dai, Suita 565-8565, Japan
e-mail: zeniya@ri.ncvc.go.jp

Introduction

Small animal single-photon emission computed tomography (SPECT) allows in vivo high-resolution three-dimensional (3D) imaging of physiological functions in small animals. This facilitates an objective assessment of the pharmaceutical development and regenerative therapy in pre-clinical studies [1–8]. However, a conventional pinhole SPECT with single circular orbit has major limitations associated with non-uniform spatial resolution or axial blurring [1, 9]. This blurring can be moderated by applying statistical image reconstruction methods such as maximum likelihood expectation maximization (MLEM) [10] or ordered subsets expectation maximization (OSEM) [11] rather than Feldkamp's filtered back-projection (Feldkamp-FBP) method [12], but still remains problematic at the periphery of field of view [1, 9]. Recently, we have demonstrated that the uniformity of spatial resolution can be improved by complete projection data acquired with two different circular orbits [13, 14] that satisfy data completeness condition

of Tuy [15], combined with 3D-OSEM. However, a long computation time is required to obtain the reconstructed image because 3D-OSEM is an iterative method and two-circular orbit acquisition doubles the size of the projection data. To reduce the long reconstruction time, we parallelized the two-orbit 3D-OSEM reconstruction process by using a personal computer (PC) cluster. Several investigators have demonstrated speed-up of 3D-OSEM reconstruction in positron emission tomography (PET) [16–19] and SPECT [20]. This study was aimed at improving the speed of the computing time for two-orbit pinhole 3D-OSEM reconstruction. We have previously succeeded in improving the performance of motion correction for PET using a Beowulf PC cluster [21]. Beowulf PC cluster (http://www.beowulf.org) is defined as a cluster of several PCs running a free-software operating system such as Linux or FreeBSD, interconnected by an Ethernet or Myrinet network. Therefore, this cluster system can be extremely inexpensively built compared with conventional super computer systems. In this study, we implemented two-orbit pinhole 3D-OSEM on our Beowulf PC cluster. To test the performance of the PC cluster, actual data were processed and compared with results obtained by a single PC.

Materials and methods

PC cluster

The Beowulf-type PC cluster consists of seven PCs. There are four 2.4 GHz Xeon processors for a master PC and dual 1.4 GHz Pentium III processors for six slave PCs connected to Gbit Ethernet switches (Fig. 1, Table 1). Each PC has 1 GB physical memory. For the parallelizing task, we installed the local area multicomputing (LAM) 6.5.7 version of the message passing interface (MPI) protocol (http://www.lam-mpi.org) on each PC.

Table 1 Specification of our Beowulf personal computer (PC) cluster

Component	Specification
Master PC	PowerEdge 2650 (Dell) 4 Xeon (Intel) 2.4 GHz 1 GB physical memory Linux 2.4.18 operating system
Slave PCs (six)	PowerEdge 1650 (Dell) Dual Pentium III (Intel) 1.4 GHz 1 GB physical memory Linux 2.4.18 operating system
Switching hub	SuperStack 3 Switch 4900 (3COM) 12 × 1000BASE-T port

The program for this system was written in the C language (gcc version 2.96) on a Linux operating system (version 2.4.18).

Theory of formulation for parallelizing two-orbit pinhole 3D-OSEM reconstruction

Figure 2 shows a schematic diagram of two-orbit pinhole SPECT geometry and two-orbit 3D-MLEM iterative reconstruction. The two-orbit 3D-MLEM update can be expressed as

$$\lambda_j^{k+1} = \frac{\lambda_j^k}{\sum_{l=1}^{2}\sum_{i=1}^{n} C_{lij}} \sum_{l=1}^{2}\sum_{i=1}^{n} \frac{y_{li} C_{lij}}{\sum_{j=1}^{m} C_{lij}\lambda_j^k}, \quad (1)$$

where λ_j^k is the value of the image voxel j for the kth iteration, y_{li} is the measured value of the projection pixel i for the lth orbit, and C_{lij} is the probability of detecting a photon originating from image voxel j at projection pixel i for the lth orbit. Each iteration of the MLEM algorithm for two orbits consists of the following four steps: (1) forward-projecting current image estimate λ_j^k for two orbits (forward-projection), (2) dividing the measured and forward projections for two orbits (correction), (3) back-projecting corrections for two orbits (back-projection), and (4) generating λ_j^{k+1} with the back-projected image. A 3D voxel-driven projector using bilinear interpolation on the detector plane was employed in both the back- and forward-projections.

The ordered subsets (OS) scheme was used to reduce the number of iterations, and subsets were evenly divided for both orbits. In our earlier studies [13, 14], as 120

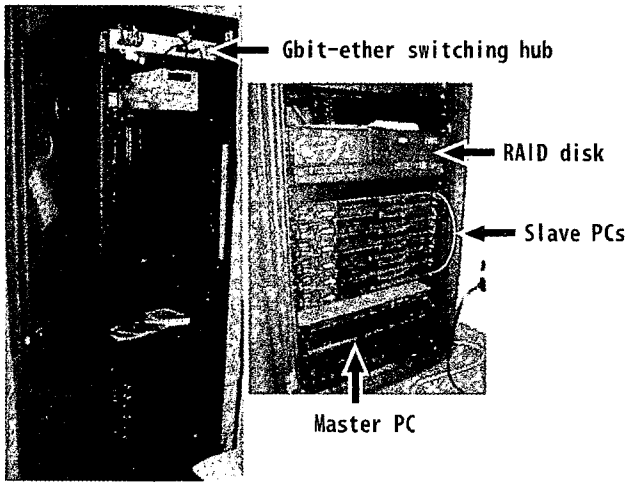

Fig. 1 Photograph of our Beowulf personal computer (PC) cluster

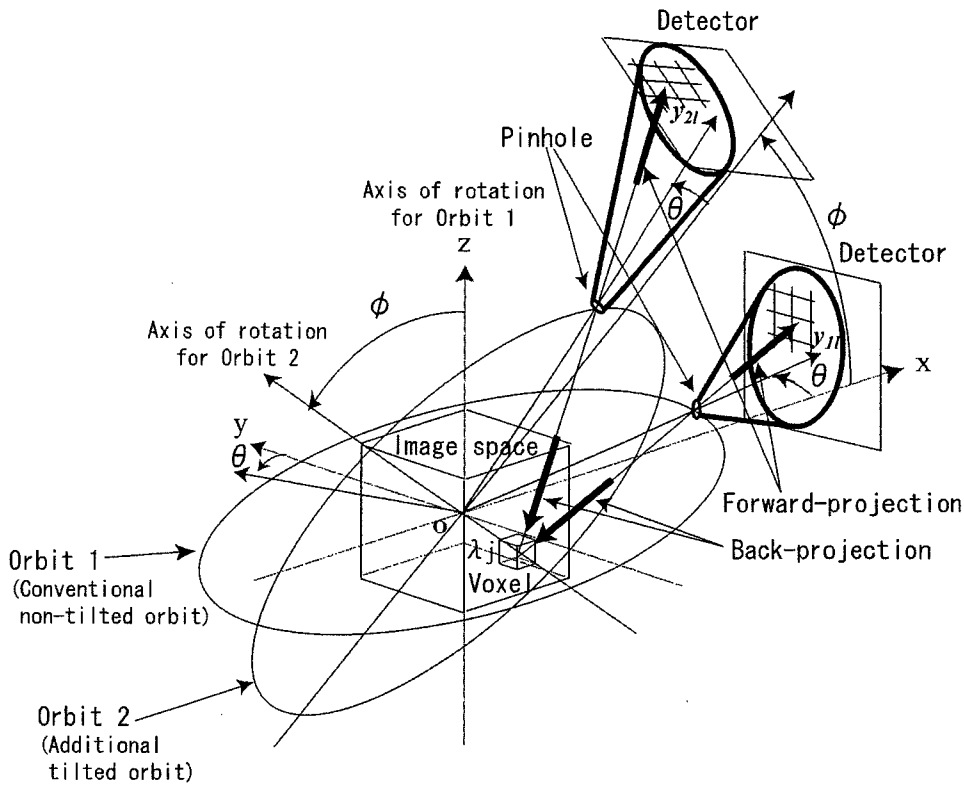

Fig. 2 Schematic diagram of geometry and three-dimensional ordered subsets expectation maximization (3D-OSEM) iterative image reconstruction in the pinhole single-photon emission computed tomography system with two-circular orbit

```
for all Iterations {
    for all Subsets{
        for (Views/Subsets) × Orbits on each PC {        Process 1: in parallel
            Forward-project current image estimate
            Calculate correction (measured projection / forward projection)
            Back-project correction
        }
        Sum partial back-projeced images on all PCs      Process 2: synchronization
        Update current image estimate (image ← image × backprojected image)
    }
}
```

Fig. 3 Pseudocode of parallelized 3D-OSEM for two orbits

projections for single orbit or 240 projections for two orbits were acquired and the current image estimate was updated with 8 subsets, 15 or 30 projections were assigned to one subset (i.e., data of $\theta = 0°, 24°, 48°, 72°, \ldots, 336°$ from both orbits were used to form the first subset).

We applied the projection space decomposition (PSD) [18] for parallelizing the two-orbit pinhole 3D-OSEM reconstruction. This method operates projection data in a block of a view. Figure 3 shows a pseudocode of parallelized 3D-OSEM for two orbits. Process 1 in Fig. 3 can be parallelized because the forward- and back-projection

Table 2 Distribution of 30-projection data in first subset to seven-PC cluster

PC number	Projection number (orbit number)				
1	1 (1)	57 (1)	113 (1)	49 (2)	105 (2)
2	9 (1)	65 (1)	1 (2)	57 (2)	113 (2)
3	17 (1)	73 (1)	9 (2)	65 (2)	
4	25 (1)	81 (1)	17 (2)	73 (2)	
5	33 (1)	89 (1)	25 (2)	81 (2)	
6	41 (1)	97 (1)	33 (2)	89 (2)	
7	49 (1)	105 (1)	41 (2)	97 (2)	

operations associated with each view are independent and can therefore proceed in parallel. At the end of each subset, a partial back-projected image is generated on each PC and these partial images are transferred to all PCs and then summed, to obtain the complete back-projected image (Process 2 in Fig. 3). Image synchronization is required for Process 2. Initial image estimates are loaded on memory on all PCs. The MPI library was used to implement this parallelization. In the MPI protocol, an identical program runs on independent PCs, with their interactions controlled by exchanging messages.

Figure 4 shows the distribution of 15 projections in one subset for single orbit in the case of total 120 projections. Table 2 shows the distribution of 30 projections in the subset for two orbits when seven PCs are used. As

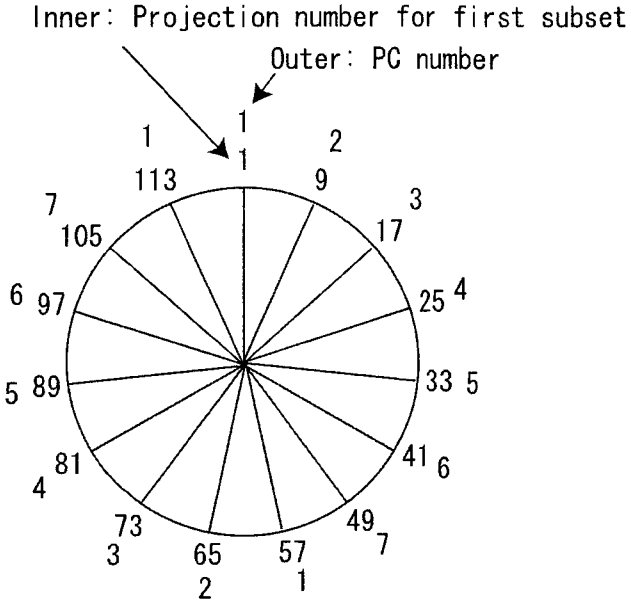

Fig. 4 Distribution of 15-projection data in the first subset for single orbit to seven-PC cluster

shown in Table 2, one PC needs to compute all 30 projections by itself, whereas with seven PC cluster each node uses five projections.

Performance evaluation using pinhole SPECT data

To evaluate the effects of parallelization, data obtained from previous phantom study were used. Detailed descriptions of the pinhole SPECT system were reported previously [13, 14]. This system consisted of a rotating object stage, a fixed conventional SPECT gamma camera (GCA-7100A, Toshiba, Tokyo, Japan) equipped with a pinhole collimator. The system can acquire two independent projection data sets with two different circular orbits to satisfy the completeness condition of Tuy. The rotating stage held the object vertically at tilted angles of $\phi = 0°$ and 45° to satisfy Tuy's condition. A multiple-disk phantom with ^{99m}Tc solution was used to evaluate axial blurring and resolution uniformity [13]. Projection data were acquired for 120 angular views in 3° steps for both orbits, in a 128 × 128 matrix with 16-bit integers. After decay correction, the total size of 240-projection data for two orbits with 32-bit floating point numbers was 15.7 MB. The projection data were reconstructed with eight subsets and two iterations, in a 128 × 128 × 128 matrix with 32-bit floating point numbers (8.4 MB).

Time for reconstruction was measured using different numbers of PCs from one to seven to evaluate the performance of the PC cluster. These measurements were repeated 10 times and the averaged reconstruction time was computed. For reference, the reconstruction time by non-iterative single-orbit Feldkamp-FBP approach was also measured. Feldkamp-FBP program provided by Toshiba was used in this study. The images reconstructed by the PC cluster and single PC were compared to verify whether they equaled. The difference of the two images was evaluated voxel by voxel by calculating the reconstruction error as

$$\varepsilon = \max_j \frac{|\lambda_j^S - \lambda_j^M|}{\lambda_j^S} \times 100(\%), \quad (2)$$

where λ_j^S is the voxel value of image obtained with single PC and λ_j^M obtained by PC cluster.

Results

Figure 5 shows the relationship between the number of PCs and the reconstruction time. The reconstruction time was reduced by increasing the number of PCs. The reconstruction time was 54 min and 18 s with a single PC, and was reduced to 10 min and 2 s with PC cluster. The speed-up factor was approximately 5.4. In this study, the reconstruction time with seven PCs was not improved compared with that with six PCs. The reconstruction time using single-orbit Feldkamp-FBP was 2 min and 44 s. The long reconstruction time by our two-orbit 3D-OSEM was greatly reduced by parallelization with PC cluster, and compared with Feldkamp-FBP, the computation time was about 7 min longer with the PC cluster whereas it was about 52 min longer with the single PC.

As shown in Fig. 6, the image reconstructed by the cluster with six PCs was virtually identical with that with the single PC, and considerably better than image by the single-orbit Feldkamp-FBP method. The reconstruction error ε for the difference between these two images was 0.0001% from Eq. 2.

Discussion

We recently demonstrated that the major limitations in conventional pinhole SPECT, namely, non-uniform spatial resolution or axial blurring in reconstruction images were dramatically improved by complete data acquired using two circular orbits, combined with 3D-OSEM iterative reconstruction. One of the drawbacks of this approach is that it takes a long time to reconstruct in compensation for excellent image from two

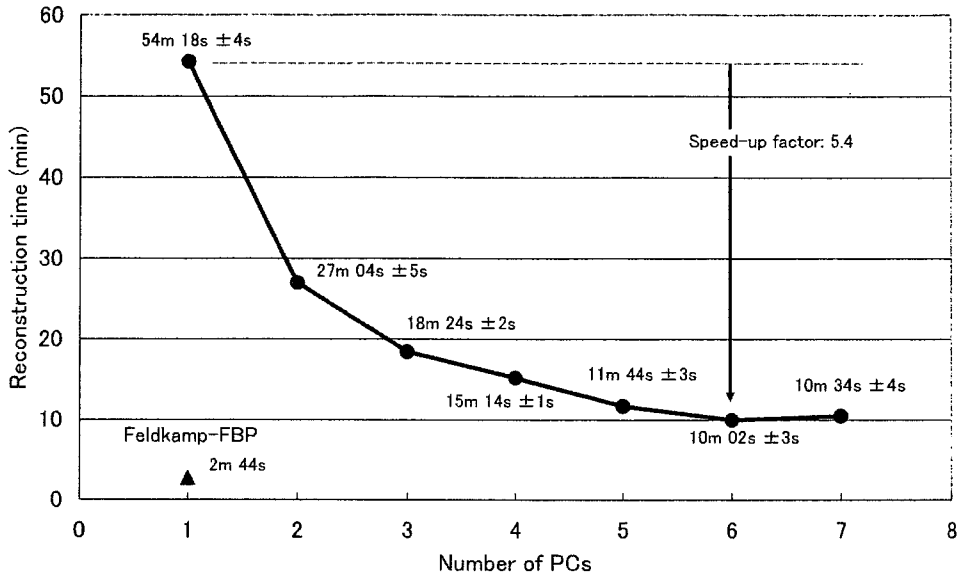

Fig. 5 Relationship between the number of PCs and reconstruction time (min) in parallel computing using the PC cluster

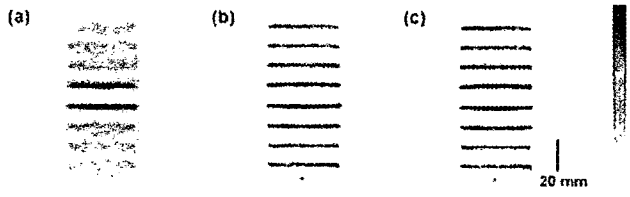

Fig. 6 Coronal images of the multiple-disk phantom reconstructed. The image (a) was reconstructed by the single-orbit Feldkamp-filtered back-projection method on single PC. The image (b) was reconstructed by the two-orbit 3D-OSEM method on single PC. The image (c) was reconstructed by the two-orbit 3D-OSEM method with PC cluster (six PCs)

independent projection data sets with two circular orbits. In this study, the long reconstruction time could be markedly reduced by parallel computing with the PC cluster. The parallelized reconstruction could be needed when resolution recovery, attenuation correction, and scatter correction are used in pinhole SPECT because they also increase the computation time [22].

The image reconstructed using the PC cluster was compared with that using the single PC. The error ε for evaluating the difference between these two images was 0.0001%, meaning that they were virtually identical. This slight error is attributed to the fact that the order of the addition of data back-projected from each view in the PC cluster is different from that in the single PC, and might have occurred during computation of the partial back-projection. However, this difference is negligible as shown by the small value of ε.

In this study, the reconstruction time with seven PCs was not improved compared with that with six PCs, as shown in Fig. 5, because the number of projections processed per one PC in the case of both six and seven PCs were equal. The partial back-projected images on each PC have to be transferred to all PCs, to sum those images on all PCs as shown in Process 2 in Fig. 3. Therefore, the communication time using seven PCs was longer than that using six PCs. The network performance is important for the Beowulf PC cluster.

This study was performed using the cluster with seven PCs. If the cluster had 30 PCs, one PC would process for only one projection. Assuming a linear model and roughly estimating from the results of this study, the reconstruction time using 30 PCs will equal that of 2–3 min with single-orbit FBP. Practically linear speed-up is not expected because back-projection is not a complete parallel process. The partial back-projected images on all PCs have to be transferred to all PCs and then summed on each PC with synchronization. We should consider that the communication time to transfer the partial images increases with increasing the number of PCs or enlarging the size of data. A high-performance communication network is essential for such cases [19]. When the size of the data is large, sufficient physical memory should be prepared to avoid memory swapping which increases the computation time.

To further improve the PC cluster, we must consider optimizing the use of each PC. In this study, there is an imbalance of the load distribution when using seven PCs. As shown in Table 2, while PC 1 and PC 2 process

for the fifth projections of the projections distributed, the other PCs are idle. If projections processed are more evenly distributed to all PCs, the speed of computation should be improved further. The reason for such a non-uniform distribution in this system is that one detector space cannot be decomposited in the combination of voxel-driven projector and PSD. There are two approaches available to evenly distribute data for all the PCs: (i) apply a ray-driven projector [23] instead of voxel-driven one for PSD because it allows the decomposition of one detector space and (ii) apply the image space decomposition method [18] for voxel-driven projector. However, further investigations are required to confirm that these alternative approaches improve the computation speed. When the cluster has slow PCs or other tasks use the resources in the cluster, the reconstruction time will increase as a result of spending too much time on slow PCs. In the present system, the fast PCs wait until the slow PCs complete the back-projection process. If the cluster system monitors the computation speed and the progress of the process on each PC and manages the distribution of the process to idle or fast PCs, the speed-down of reconstruction will be avoided [16].

At present we do not parallelize for one PC with multiple processors. Because the multiple processors on one PC can share memory, communication through the network for summing partial images is unnecessary [16]. Shattuck et al. [17] reported that a four-processor computer was able to achieve speed-up factors of approximately 3.4 relative to a single processor. Parallelization for both cluster PCs and multiple processors will effectively speed up the reconstruction time.

The Beowulf PC cluster system can be constructed using essentially free-software such as Linux operating system and MPI, and inexpensive PCs instead of super computer. Also, modifications of only approximately 10 lines were required to parallelize the reconstruction program. Although this article describes parallelization for the two-orbit pinhole SPECT, the strategy can be generalized for any pinhole SPECT (e.g., single orbit, helical orbit, and multipinholes).

Conclusions

We were able to markedly improve the long computation time of 3D-OSEM reconstruction in two-circular orbit pinhole SPECT by parallel computing using the PC cluster. The reconstruction time of 54min decreased to 10min by using six PCs. The speed-up factor was 5.4. The PC cluster is effective in decreasing the computing time with low cost and easy construction.

Acknowledgment This study was partly supported by the Japan Science and Technology Agency (JST).

References

1. Jaszczak RJ, Li J, Wang H, Zalutsky MR, Coleman RE. Pinhole collimation for ultra-high-resolution, small-field-of-view SPECT. Phys Med Biol 1994;39:425–37.
2. Weber DA, Ivanovic M, Franceschi D, Strand SE, Erlandsson K, Franceschi M, et al. Pinhole SPECT: an approach to in vivo high resolution SPECT imaging in small laboratory animals. J Nucl Med 1994;35:342–8.
3. Ishizu K, Mukai T, Yonekura Y, Pagani M, Fujita T, Magata Y, et al. Ultra-high resolution SPECT system using four pinhole collimators for small animal studies. J Nucl Med 1995;36:2282–7.
4. Ogawa K, Kawade T, Nakamura K, Kubo A, Ichihara T. Ultra high resolution pinhole SPECT for small animal study. IEEE Trans Nucl Sci 1998;45:3122–6.
5. Hirai T, Nohara R, Ogoh S, Chen LG, Kataoka K, Li XH, et al. Serial evaluation of fatty acid metabolism in rats with myocardial infarction by pinhole SPECT. J Nucl Cardiol 2001;8:472–81.
6. Scherfler C, Donnemiller E, Schocke M, Dierkes K, Decristoforo C, Oberladstätter M, et al. Evaluation of striatal dopamine transporter function in rats by in vivo β-[^{123}I]CIT pinhole SPECT. Neuroimage 2002;17:128–41.
7. Acton PD, Choi SR, Plössl K, Kung HF. Quantification of dopamine transporters in the mouse brain using ultra-high resolution single-photon emission tomography. Eur J Nucl Med 2002;29:691–8.
8. Aoi T, Watabe H, Deloar HM, Ogawa M, Teramoto N, Kudomi N, et al. Absolute quantitation of regional myocardial blood flow of rats using dynamic pinhole SPECT. In: Conference Record of 2002 IEEE Nuclear Science Symposium and Medical Imaging Conference (CD-ROM), 2003. p. 1780–3.
9. Vanhove C, Defrise M, Franken PR, Everaert H, Deconinck F, Bossuyt A. Interest of the ordered subsets expectation maximization (OS-EM) algorithm in pinhole single-photon emission tomography reconstruction: a phantom study. Eur J Nucl Med 2000;27:140–6.
10. Shepp LA, Vardi Y. Maximum likelihood reconstruction for emission tomography. IEEE Trans Med Imag 1982;MI-1: 113–22.
11. Hudson HM, Larkin RS. Accelerated image reconstruction using ordered subsets of projection data. IEEE Trans Med Imag 1994;13:601–9.
12. Feldkamp LA, Davis LC, Kress JW. Practical cone-beam algorithm. J Opt Soc Am A 1984;1:612–9.
13. Zeniya T, Watabe H, Aoi T, Kim KM, Teramoto N, Hayashi T, et al. A new reconstruction strategy for image improvement in pinhole SPECT. Eur J Nucl Med Mol Imaging 2004: 31:1166–72.
14. Aoi T, Zeniya T, Watabe H, Deloar HM, Matsuda T, Iida H. System design and development of a pinhole SPECT system for quantitative functional imaging of small animals. Ann Nucl Med 2006;20:245–51.
15. Tuy HK. An inversion formula for cone-beam reconstruction. SIAM J Appl Math 1983;43:546–52.
16. Vollmar S, Michel C, Treffert JT, Newport DF, Casey M, Knöss C, et al. *HeinzelCluster*: accelerated reconstruction for FORE and OSEM3D. Phys Med Biol 2002;47:2651–8.

17. Shattuck DW, Rapela J, Asma E, Chatzioannou A, Qi J, Leahy RM. Internet2-based 3D PET image reconstruction using a PC cluster. Phys Med Biol 2002;47:2785–95.
18. Jones JP, Jones WF, Kehren F, Newport DF, Reed JH, Lenox MW, et al. SPMD cluster-based parallel 3-D OSEM. IEEE Trans Nucl Sci 2003;50:1498–502.
19. Jones JP, Jones WF, Everman J, Panin V, Michel C, Kehren F, et al. Impact of a high-performance communication network on cluster-based parallel iterative reconstruction. In: Conference Record of 2005 IEEE Nuclear Science Symposium and Medical Imaging Conference (CD-ROM), 2006. p. 2273–7.
20. Rong Z, Tianyu M, Yongjie J. Parallel OSEM reconstruction algorithm for fully 3-D SPECT on a Beowulf cluster. Conf Proc IEEE Eng Med Biol Soc 2005;2:1834–7.
21. Watabe H, Woo SK, Kim KM, Kudomi N, Iida H. Performance improvement of event-based motion correction for PET using a PC cluster. In: Conference Record of 2003 IEEE Nuclear Science Symposium and Medical Imaging Conference (CD-ROM), 2004. p. 2407–9.
22. Sohlberg A, Watabe H, Zeniya T, Iida H. Comparison of multi-ray and point-spread function based resolution recovery methods in pinhole SPECT reconstruction. Nucl Med Commun 2006;27:823–7.
23. Sohlberg A, Ruotsalainen U, Watabe H, Iida H, Kuikka JT. Accelerated median root prior reconstruction for pinhole single-photon emission tomography (SPET). Phys Med Biol 2003;48:1957–69.

Stroke
JOURNAL OF THE AMERICAN HEART ASSOCIATION

American Stroke Association
A Division of American Heart Association

Delayed Postischemic Treatment With Fluvastatin Improved Cognitive Impairment After Stroke in Rats

Munehisa Shimamura, Naoyuki Sato, Masataka Sata, Hitomi Kurinami, Daisuke Takeuchi, Kouji Wakayama, Takuya Hayashi, Hidehiro Iida and Ryuichi Morishita

Stroke published online Nov 1, 2007;
DOI: 10.1161/STROKEAHA.107.485045
Stroke is published by the American Heart Association. 7272 Greenville Avenue, Dallas, TX 72514
 Print ISSN: 0039-2499. Online ISSN: 1524-4628

Delayed Postischemic Treatment With Fluvastatin Improved Cognitive Impairment After Stroke in Rats

Munehisa Shimamura, MD, PhD; Naoyuki Sato, MD, PhD; Masataka Sata, MD, PhD; Hitomi Kurinami, MD; Daisuke Takeuchi, MD; Kouji Wakayama, MD; Takuya Hayashi, MD, PhD; Hidehiro Iida, MD, PhD; Ryuichi Morishita, MD, PhD

Background and Purposes—Recent clinical evidences indicate that statins may have beneficial effects on the functional recovery after ischemic stroke. However, the effect of delayed postischemic treatment with statins is still unclear. In the present study, we evaluated the effects of fluvastatin in the chronic stage of cerebral infarction in a rat model.

Methods—Rats exposed to permanent middle cerebral artery occlusion were treated for 3 months with fluvastatin beginning from 7 days after stroke. MRI, behavioral analysis, and immunohistochemistry were performed.

Results—Two months of treatment with fluvastatin showed the significant recovery in spatial learning without the decrease in serum total cholesterol level and worsening of infarction. Microangiography showed a significant increase in capillary density in the peri-infarct region in fluvastatin-treated rats after 3 months of treatment. Consistently, BrdU/CD31-positive cells were significantly increased in fluvastatin-treated rats after 7 days of treatment. MAP1B-positive neurites were also increased in the peri-infarct region in fluvastatin-treated rats. In addition, rats treated with fluvastatin showed the reduction of superoxide anion after 7 days of treatment and the reduction of Aβ deposits in the thalamic nuclei after 3 months of treatment.

Conclusions—Thus, delayed postischemic administration of fluvastatin had beneficial effects on the recovery of cognitive function without affecting the infarction size after ischemic stroke. Pleiotropic effects of fluvastatin, such as angiogenesis, neuritogenesis, and inhibition of superoxide production and Aβ deposition, might be associated with a favorable outcome. (***Stroke.*** **2007;38:000-000.)**

Key Words: angiogenesis ■ cerebral infarct ■ microcirculation ■ statins

Despite conflicting data correlating cholesterol level with stroke, 2 early trials of HMG-CoA reductase inhibitors (statins) in patients after myocardial infarction patients showed a reduction in stroke risk as a secondary end point.[1] A meta-analysis of 9 statin intervention trials, which enrolled patients with coronary artery disease or those at high risk for coronary disease, demonstrated a 21% relative risk reduction for stroke after 5 years of treatment.[2] Another clinical evidence suggests that the commencement of statins within 4 weeks of a stroke results in a favorable 90-day outcome.[3] To clarify the effects of postischemic statin treatment, previous studies in which atorvastatin was started 1 day after stroke in rodents showed improvement of sensory motor deficit through induction of angiogenesis, neurogenesis, and synaptogenesis.[4,5] These pleiotropic effects of statins were shown to be the result of induction of vascular endothelial growth factor or brain-derived neurotrophic factor.[4] Additionally, the microvascular dysfunction in the posttreatment of stroke with recombinant human tissue-type plasminogen activator could be reduced by statins in rodent model.[6] However, the effect of delayed treatment with statins after ischemic stroke is still unknown. From this viewpoint, we investigated whether chronic statin treatment beginning 7 days after ischemic stroke had influences on neurological deficits and pathophysiology after the permanent middle cerebral artery occlusion (MCAo) model in rats.

Materials and Methods

Surgical Procedure

Male Wistar rats (270 to 300 grams; Charles River; Kanagawa, Japan) were used in this study. The right MCA was occluded by placement of poly-L-lysine–coated 4-0 nylon, as described previously.[7]

Protocol for Treatment and Behavioral Tests

Ten rats were only anesthetized (sham operation) and 32 rats were subjected to MCAo (day 1). Based on neuromuscular function on day 7, the rats were divided equally into saline-treated (n=16) or fluvastatin-treated (n=16) groups. Fluvastatin (5 mg/kg per day;

Received February 14, 2007; final revision received April 27, 2007; accepted May 30, 2007.

From Department of Advanced Clinical Science and Therapeutics (M.S., M.Sata, K.W.), Graduate School of Medicine, the University of Tokyo, Japan; Department of Clinical Gene Therapy (N.S., H.K., D.T., R.M.), Graduate School of Medicine, Osaka University, Japan; Department of Investigative Radiology (T.H., H.I.), National Cardiovascular Center, Research Institute, Japan.

Correspondence to Ryuichi Morishita, MD, PhD, Professor, Division of Clinical Gene Therapy, Graduate School of Medicine, Osaka University, 2-2 Yamada-oka, Suita 565-0871, Japan. E-mail morishit@cgt.med.osaka-u.ac.jp

Stroke is available at http://stroke.ahajournals.org

DOI: 10.1161/STROKEAHA.107.485045

provided by Novartis Pharma) or saline was given by gavage from day 7 to 100. We chose the dose (5 mg/kg per day), because a previous report showed that this dose could effectively induce angiogenesis in ischemic limb.[8] On day 55, neuromuscular function and locomotor activity were evaluated in the surviving rats. Then, cognitive function was examined by Morris water maze from day 56 to 63, because the effects of neuronal regeneration could be detected not in the early stage but in the chronic stage of ischemic brain such as 49 to 53 days after the insult.[9] On day 96, MRI was performed. On day 100, microangiography was performed.

MRI

High-resolution T1-weighted fast spin echo sequence images (repetition time [TR]=1500 ms; echo time [TE]=10.3 ms; field of view [FOV]=4× 3 cm; matrix=256×192; slice thickness=1.5 mm; slice gap=0.5 mm; number of slices=16; number of excitation=10; total time=9.39 min) were obtained using a 3-T MRI scanner (Signa LX VAH/I; GE).

Sensory Motor Deficit and Locomotor Activity

Although there are various batteries for testing sensory motor deficit, we used a simple protocol.[10] For forelimb flexion, rats were held by the tail on a flat surface. Paralysis of the forelimbs was evaluated by the degree of left forelimb flexion. For torso twisting, rats were held by the tail on a flat surface. The degree of body rotation was checked. For lateral push, rats were pushed either left or right. Rats with right MCA occlusion showed weak or no resistance against a left push. For hind limb placement, one hind limb was removed from the surface. Rats with right MCA occlusion showed delayed or no replacement of the hind limb when it was removed from the surface.

Spontaneous activity was measured via the open field (0.69 m^2). We set the sensor, which also put beams on the field, at 30 cm above the field. The number of count, which is when the animal crosses the beam, was measured for 30 minutes.

Morris Water Maze Task

A cylindrical tank 1.5 m in diameter was filled with water (25°C), and a transparent platform 15 cm in diameter was placed at a fixed position in the center of 1 of the 4 quadrants (O'Hara & Co, Ltd). In the hidden platform trials, we performed the tests 4 times per day for 4 days. When the rat could not reach the platform, the latency was set at 60 sec. In the visible platform trials, the tests were performed 4 times per day for 4 days. The acquired data were averaged per day.

Evaluation of Capillary Density

Using a recently developed microangiographic technique,[11] capillary density and blood–brain barrier leakage were evaluated in the cerebral cortex after MCA occlusion. The area or length of vessels was analyzed with an angiogenesis image analyzer (version 1.0; Kurabo).

Immunohistochemical Study: Bromodeoxyuridine Labeling

To identify newly formed DNA, saline-treated (n=5) and fluvastatin-treated (n=5) rats received injections of bromodeoxyuridine (BrdU, 50 mg/kg; Sigma-Aldrich, Saint Louis, Mo) intraperitoneally starting on day 7 twice per day until day 13. Rats were euthanized on day 14. After the sections (8-μm thickness) was fixed in 10% formaldehyde/MeOH neutral buffer solution and blocked, they were incubated with mouse monoclonal anti-rat CD31 antibody (1:100; BD Biosciences; San Jose, Calif), goat polyclonal anti-doublecortin (anti-DCX; Santa Cruz) antibody (1:100; Santa Cruz, Calif), mouse monoclonal anti-NeuN antibody (1:1000; Chemicon, Temecula, Calif), or mouse monoclonal anti-MAP1B antibody (1:100; Sigma-Aldrich), followed by anti-mouse goat fluorescent antibody (1:1000 for NeuN and MAP1B, 1:400 for CD31, Alexa Flour 546, Molecular Probes; Eugene, Ore) or anti-goat donkey fluorescent antibody (1:1000 for DCX Alexa Fluor 546). For double immunostaining, these sections were fixed again and incubated in 2 N HCl at 37°C for 30 minutes. After blocking, they were incubated with rat monoclonal anti-BrdU antibody (1:200; Abcam, Cambridge, UK) followed by anti-rat goat fluorescent antibody (1:1000, Alexa Fluor 488). For immunohistochemical staining for Aβ, sections were pretreated for 30 minutes with hot (85°C) citrate buffer as described before.[12] Confocal images were acquired using an FV-300 (Olympus).

Table. Infarction Volume Calculated by MRI, Blood Pressure, and Serum Total Cholesterol

	Sham	MCAo+S	MCAo+F	*P*
Infarction volume in total rats (mm^3)	...	283.8±23.9	278.4±26.4	0.851
Type of infarction in Figure 1a (N of rats)				0.828
A	...	12	11	...
B	...	3	3	...
C	...	1	2	...
Infarction volume (mm^3) in type A rats	...	322.8±15.0	327.0±18.8	0.758
Systolic blood pressure (mm Hg) in type A rats				
Day 7	116.1±5.4	123.7±6.0	115.5±7.3	0.654
Day 56	146.5±4.7	148.3±2.7	136.1±5.2	0.132
Serum total cholesterol (mg/dl) in type A rats on day 56	85.9±5.6	75.3±3.5	73.5±2.7	0.949

Type A, low-intensity area seen in the dorsolateral and lateral portions of the neocortex and the entire caudate putamen; type B, low-intensity area seen in the dorsolateral and lateral portions of the neocortex and in part of the caudate putamen; type C, low-intensity area seen in part of the lateral neocortex and caudate putamen. MCAo+S, saline-treated rats after MCAo; MCAo+F, fluvastatin-treated rats after MCAo.

P, saline vs fluvastatin.

Quantitative Histological Analysis

To quantify the immunoreactivity for MAP1B and Aβ, the acquired image was analyzed by Image J (version 1.32; NIH).

Detection of Superoxide Anion in Brain Sections

Superoxide anion was detected on day 14 as described previously.[13] Because intact cortex showed red fluorescence, we calculated the ratio of fluorescence as follows: ratio of fluorescence=[fluorescence intensity in ischemic core or peri-infarct region]/[fluorescence intensity in intact region].

Statistical Analysis

All values are expressed as mean±SEM. To analyze the differences in the type of cerebral infarction, χ^2 test was performed. The latency, path length, and mean speed in Morris water maze and sensory motor deficits were analyzed by a 2-factor repeated-measure ANOVA. Post hoc analyses were performed, and the Scheffe test was applied to control the inflation in type I error. The value of the serum total cholesterol, the blood pressure, and the spontaneous activity was analyzed by Scheffe rules. The differences in the immunohistochemistry and the volume of infarction were assessed by Mann–Whitney *U* analyses. In all cases, $P<0.05$ was considered significant.

Results

Effects of Fluvastatin on Cognitive Impairment

To confirm the severity of cerebral infarction, all rats were examined by T1-weighted MRI after 89 days of treatment. Although the total volume of infarction calculated in T1-weighted images was not different between rats treated with

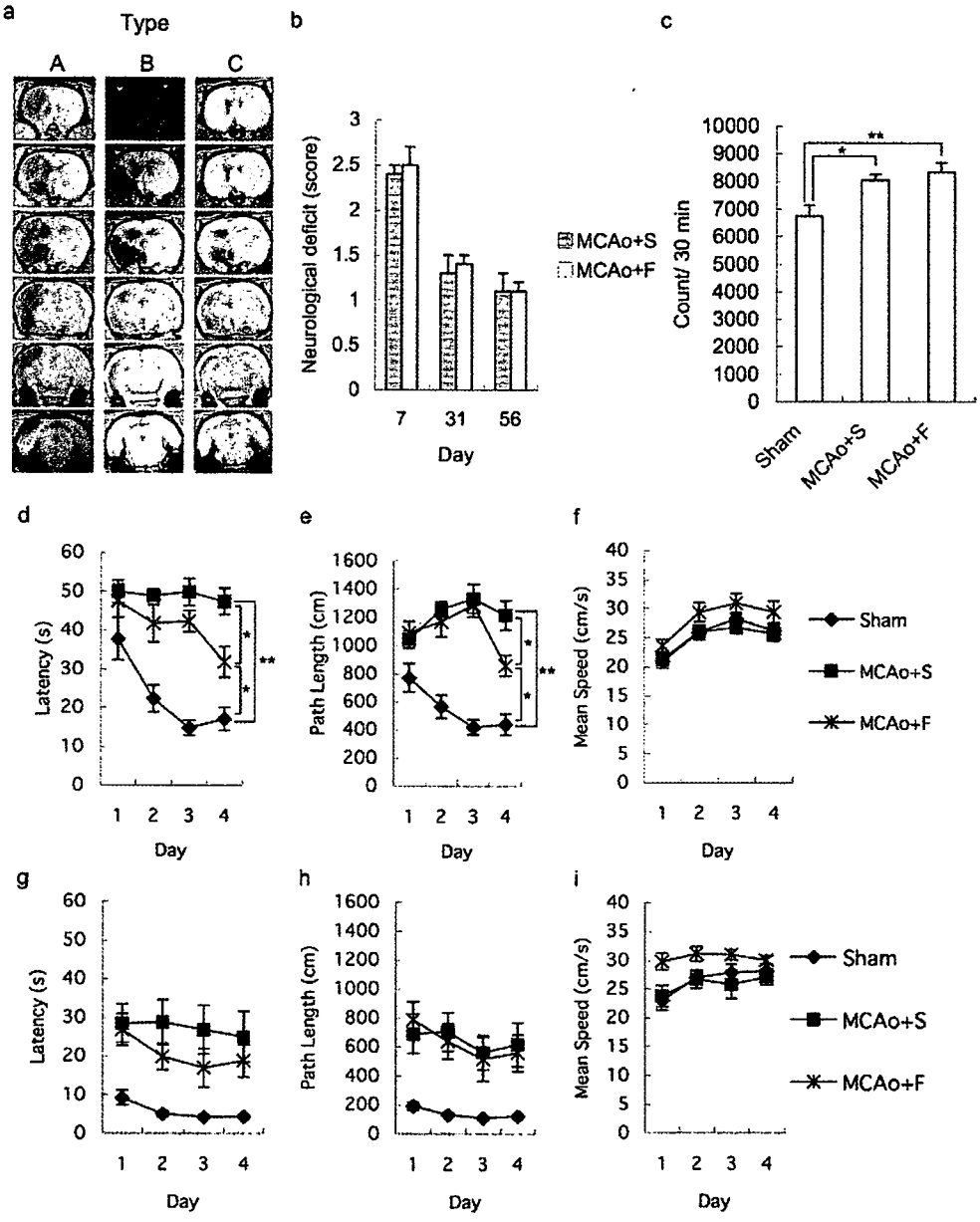

Figure 1. Typical T1-weighted image of coronal section of rat brain (a). The images were divided into 3 groups. Type A, low-intensity area seen in the dorsolateral and lateral portions of neocortex and the entire caudoputamen; type B, low-intensity area seen in the dorsolateral and lateral portions of neocortex and in part of the caudatoputamen; and type C, high-intensity area seen in part of the lateral neocortex and caudatoputamen. Sensory motor deficit (b). Spontaneous locomotor activity (c). Hidden platform test in Morris water maze. Each figure showed latency (d), path length (e), and mean speed (f). Days 1 to 4 indicate the trial day in the hidden platform test (56 to 59 days after middle cerebral artery occlusion). Visible platform test in Morris water maze. Each figure showed latency (g), path length (h), and mean speed (i). Days 1 to 4 indicate the day in the visible platform test (60 to 63 days after middle cerebral artery occlusion). MCAo+S indicates rats treated with saline after middle cerebral artery occlusion; MCAo+F, rats treated with fluvastatin after middle cerebral artery occlusion.

saline and fluvastatin (Table), the pattern of cerebral infarction was divided into 3 groups: type A, low-intensity area seen in the dorsolateral and lateral portions of the neocortex and the entire caudate putamen; type B, low-intensity area seen in the dorsolateral and lateral portions of the neocortex and in part of the caudate putamen; type C, low-intensity area seen in part of the lateral neocortex and caudate putamen (Figure 1a). In type C, most of the lateral neocortex was intact. To exclude the influence of the pattern of cerebral infarction on cognitive function, we focused on type A rats in the present study. The volume of cerebral infarction in type A rats was not different between the groups (Table). Blood pressure and serum total cholesterol also showed no difference among the groups (Table).

Sensory motor deficit had spontaneously recovered to some extent by 8 weeks in both groups, and there was no difference (Figure 1b). Locomotor activity in rats subjected to MCAo was increased as compared with that in sham-operated rats, as described before,[14] but there was no significant difference between fluvastatin-treated and saline-treated rats (Figure 1c). In Morris water maze (Figure 1d-i), which examines spatial learning, there were significant differences